ResearchGate

See discussions, stats, and author profiles for this publication at: https://www.researchgate.net/publication/302916175

Laser printing of resonant plasmonic nanovoids

Article *in* Nanoscale · January 2016

Impact Factor: 7.39 · DOI: 10.1039/C6NR01317A

READS

23

11 authors, including:

Aleksandr Kuchmizhak

Far Eastern Federal University

28 PUBLICATIONS **95** CITATIONS

SEE PROFILE

Sergey Vladimirovich Makarov

ITMO University

78 PUBLICATIONS **390** CITATIONS

SEE PROFILE

Valentin A. Milichko

ITMO University

29 PUBLICATIONS **29** CITATIONS

SEE PROFILE

Vasily V. Zhakhovsky

All-Russia Research Institute of Automatics …

149 PUBLICATIONS **1,245** CITATIONS

SEE PROFILE

Available from: Aleksandr Kuchmizhak

Retrieved on: 29 May 2016

CrossMark
click for updates

View Article Online
View Journal

Nanoscale

Accepted Manuscript

This article can be cited before page numbers have been issued, to do this please use: A. Kuchmizhak, O. Vitrik, Y. N. Kulchin, D. Stozhenko, A. Mayor, A. Mirochnik, S. Makarov, V. Milichko, S. I. Kudryashov, N. Inogamov and V. Zhakhovsky, *Nanoscale*, 2016, DOI: 10.1039/C6NR01317A.

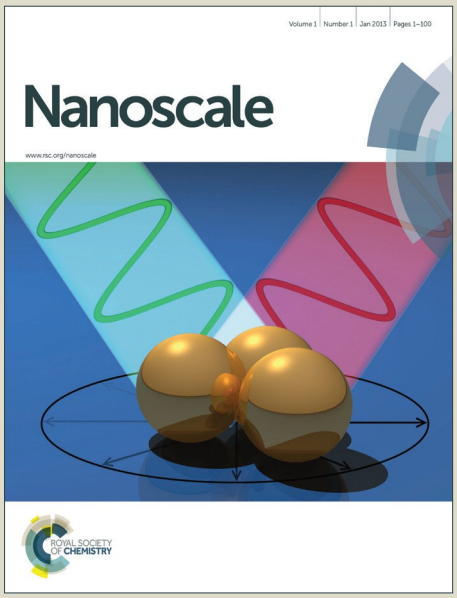

This is an *Accepted Manuscript*, which has been through the Royal Society of Chemistry peer review process and has been accepted for publication.

Accepted Manuscripts are published online shortly after acceptance, before technical editing, formatting and proof reading. Using this free service, authors can make their results available to the community, in citable form, before we publish the edited article. We will replace this *Accepted Manuscript* with the edited and formatted *Advance Article* as soon as it is available.

You can find more information about *Accepted Manuscripts* in the Information for Authors.

Please note that technical editing may introduce minor changes to the text and/or graphics, which may alter content. The journal's standard Terms & Conditions and the Ethical guidelines still apply. In no event shall the Royal Society of Chemistry be held responsible for any errors or omissions in this *Accepted Manuscript* or any consequences arising from the use of any information it contains.

ROYAL SOCIETY OF CHEMISTRY

www.rsc.org/nanoscale

Please do not adjust margins

View Article Online
DOI: 10.1039/C6NR01317A

Nanoscale

ARTICLE

Laser printing of resonant plasmonic nanovoids

A. Kuchmizhak,[a,b,†] O. Vitrik,[a,b] Yu. Kulchin,[b] D. Storozhenko,[b] A. Mayor,[b] A. Mirochnik,[c] S. Makarov,[d] V. Milichko,[d] S. Kudryashov,[d,e] V. Zhakhovsky,[f] N. Inogamov,[f,g]

Received 00th Febrary 2016,
Accepted 00th January 20xx

DOI: 10.1039/x0xx00000x

www.rsc.org/

Hollow reduced-symmetry resonant plasmonic nanostructures possess pronounced tunable optical resonances in UV-vis-IR range, being a promising platform for advanced nanophotonic devices. However, the present fabrication approaches require several consecutive technological steps to produce such nanostructures, making their large-scale fabrication rather time-consuming and expensive. Here, we report on direct single-step fabrication of large-scale arrays of hollow parabolic- and cone-shaped nanovoids in silver and gold thin films, using single-pulse femtosecond nanoablation at high repetition rates. Lateral and vertical size of such nanovoids was found to be laser energy-tunable. Resonant light scattering from individual nanovoids was observed in visible spectral range, using dark-field confocal microspectroscopy, with the size-dependent resonant peak positions. These colored geometric resonances in the far-field scattering were related to excitation and interference of transverse surface plasmon modes in nanovoid shells. Plasmon-mediated electromagnetic field enhancement near the nanovoids was evaluated via finite-difference time-domain calculations for their model shapes simulated by three-dimensional molecular dynamics, and experimentally verified by means of photoluminescence microscopy and Raman spectroscopy.

Introduction

Over the past decade considerable efforts were applied for efficient manipulation of electromagnetic fields at nanoscale through state-of-the-art design of different plasmonic nanostructures. In particular, fabrication and spectral characterization of hollow reduced-breaking plasmonic nanostructures including nanocaps [1], nanoshells [2], nanovoids [3], nanocups [4,5] are of increasing scientific interest. Such plasmonic nanostructures demonstrate pronounced light-bending, absorption and scattering properties [6,7,8] and sharper plasmon resonances [3,9,10], which spectral positions can be readily tuned over UV, visible and near-IR spectral regions via variation of shape and size of individual nanostructures [11-13]. Large-scale ordered arrays of such hollow nanostructures is a promising platform for fundamental research on excitation and interaction of different relevant localized and delocalized plasmon modes, their bandgaps and hybridization, providing deeper insight into nanoscale light-matter interaction [3]. Such ordered nanostructures can be also used as elements of active plasmonic switchers [14], nanophotonic devices [15], second-harmonic generators [16], advanced solar cells [17,18], hydrophobic surfaces [19,20] as well as sensitive elements for surface-enhanced fluorescence and Raman spectroscopy (SERS) biosensors [9,10,21,22].

Different approaches were suggested in fabrication of highly ordered arrays of hollow plasmonic nanostructures on various substrates, including combinations of electron (ion) beam treatment, followed by potassium hydroxide etching [3] or chemical synthesis [6], microsphere or porous anodic alumina template-assisted self-assembly and electrochemical deposition [23-25], etc. However, each of these approaches is requiring several consecutive technological fabrication procedures to produce such nanostructured substrates, making their large-scale fabrication rather time-consuming and expensive regarding current demands for cheap and green fabrication of biosensing substrates [26]. In contrast, femtosecond laser nanoablation is proven to be a versatile tool for "green" and high-throughput fabrication of hollow nano- and micro-scale conical-shaped voids (bumps) in thin metal films [27,28]. However, plasmonic resonant properties of such reduced-symmetry and easy-to-do nanostructures were not studied yet.

In this paper, we report a systematic parametric study on fabrication and plasmonic characterization of hollow metallic nanovoids on dielectric and silicon substrates, using nanoscale femtosecond (fs) laser ablation of thin supported films of noble metals. In this research, single tightly focused femtosecond laser pulse was demonstrated by Two-Temperature Hydrodynamic Molecular-Dynamic Monte-Carlo (2T-HD-MD-MC) simulations to initiate fast melting, detaching, deformation and rapid

[a]School of Natural Sciences, Far Eastern Federal University, 8 Sukhanova str., Vladivostok 690041, Russia
[b]Institute of Automation and Control Processes, Far Eastern Branch, Russian Academy of Science, Vladivostok 690041, Russia
[c]Institute of Chemistry, Far Eastern Branch, Russian Academy of Science, Vladivostok, 690022, Russia
[d]ITMO University, St. Petersburg 197101, Russia
[e]Lebedev Physical Institute, Russian Academy of Science, Moscow 119991, Russia
[f]Dukhov Research Institute of Automatics (SC Rosatom), 127055 Moscow, Russian Federation
[g]Landau Institute for Theoretical Physics, Russian Academy of Sciences, Chernogolovka, Russian Federation
† alex.iacp.dvo@mail.ru.

Electronic Supplementary Information (ESI) available. Sections: 1) Eu^{3+}(TTA) synthesis and optical properties; 2) SERS Enhancement factor calculations; 3) Features of the Ag nanovoid formation; 4) Nanovoid printing on the Si substrate; 5) Dark-field microspectroscopy details; 6) Effective refractive index estimations; 7) Calculated E-field distributions near the parabolic-shaped nanovoids; 8) Plasmonic PL enhancement for the parabolic- and conical-shaped nanovoids. Figures S1-S7. See DOI: 10.1039/x0xx00000x

Published on 10 May 2016. Downloaded by Middle East Technical University (Orta Dogu Teknik U) on 10/05/2016 10:26:07.

Nanoscale Accepted Manuscript

Please do not adjust margins

View Article Online
DOI: 10.1039/C6NR01317A

Published on 10 May 2016. Downloaded by Middle East Technical University (Orta Dogu Teknik U) on 10/05/2016 10:26:07.

resolidification of a noble metal film, covering glass or Si substrates, to result in both parabolic and quasi-conical hollow nanofeatures, which geometrical dimensions can be varied by changing laser pulse energy. The fabricated plasmonic nanostructures demonstrate tuneable size-dependent resonant light scattering in the visible spectral range. These color far-field scattering resonances were attributed to optical excitation and interference of relevant surface plasmon modes in nanovoid shells, providing corresponding near-field plasmon-mediated electromagnetic (EM) field enhancement, which was measured experimentally by means of photoluminescence (PL) microscopy and surface-enhanced Raman spectroscopy (SERS). In support, finite-difference time-domain (FDTD) electromagnetic calculations were performed to evaluate the range of achievable field enhancement magnitudes, using nanovoid dimensions predicted by the 2T-HD-MD-MC approach. This research provides a basis for large-scale, cost-effective and single-step fabrication of ordered arrays of simple, robust and efficient plasmonic elements, using ultrahigh (MHz-range) repetition-rate femtosecond lasers.

Experimental

Film preparation. 50-nm thick silver and gold films were deposited onto optically smooth bulk glass or Si substrates at the pressure of $5{\cdot}10^{-6}$ bar and the average speed ~8 Å/c by an e-beam evaporation procedure (Ferrotec EV M-6). The substrates were pre-cleaned with a build-in ion source (KRI EH200) to increase adhesion of the metal films. No additional adhesive layers were used. The resulting film thickness was measured by a calibrated piezoelectric resonator (Sycon STC-2002) mounted inside the vacuum chamber, and verified by atomic force microscopy measurements (NanoDST, Pacific Nanotechnologies).

Laser processing. Laser nanostructuring of the Ag and Au films on the glass or Si substrates was carried out at the 532-nm wavelength of 200-fs laser pulses, generated by an optical parametric amplifier (OPA, TOPAS prime, Spectra Physics), which was pumped by a Ti:Sapphire laser system, comprised by an oscillator (Tsunami) and an amplifier (Spitfire, Spectra Physics). The output pulses from the OPA (Fig.1(A)) via a fiber coupler, consisting of a micro-positioner and a focusing lens (NA = 0.25), were introduced into a segment of a single-mode optical fiber (Thorlabs SM400) to provide its mode filtering to a Gaussian-like beam. The filtered laser beam was then focused onto the sample surface by a high-NA lens (x100, NA = 0.95, Nikon), completely filling its input aperture, to yield in a focal spot with a 1/e-radius R_{opt} ~ 0.34 μm.

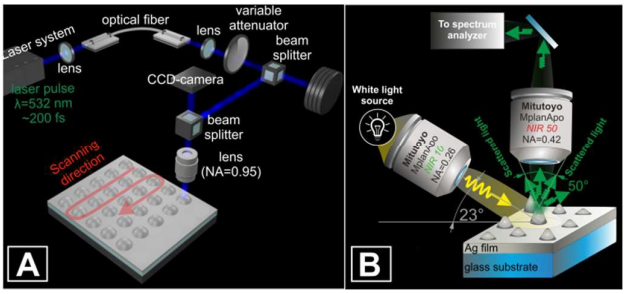

Fig.1. Single-pulse fabrication of hollow noble-metal nanovoids. (A) Schematic of the experimental setup for single-pulse nanoablation; (B) Detection scheme for dark-field scattering from single nanovoid.

The sample was mounted on a PC-driven micropositioning platform (Newport XM or GTS series), providing a minimal translation step of 50 nm along all three axes. The laser pulse energy E was varied by means of a variable attenuator and measured by a sensitive pyroelectric photodetector (Coherent J-J-10SI-HE photodetector or Coherent EPM2000 Energy meter). The resulting nanostructures were characterized, using a scanning electron microscope (SEM, JEOL 7001F) and an atomic force microscope (NanoDST, Pacific Nanotechnologies) with ultra-thin cantilevers (NT MDT 01_DLC and NSC05_10°).

Optical characterization. Spectral properties of the fabricated nanostructures in the visible spectral range were probed using dark-field (DF) optical microspectroscopy. Broadband radiation from a halogen lamp (HL 2000 FHSA) (Fig. 1B) was focused by a lens (Mitutoyo MPlanApo NIR 10, NA=0.26) onto a surface at an angle of incidence of 67° to the surface normal. The light scattered by single nanostructure was collected by a second, normally aligned objective (Mitutoyo MPlanApo NIR 50, NA=0.42) and then analyzed, using a confocal spectrometer (HORIBA LabRam HR, cooled CCD Andor DU 420A-OE 325, 150 g/mm grating).

To measure plasmonic enhancement near the nanovoids and to evaluate their sensing capabilities, they were covered by a 10-nm thick layer of Rhodamine 6G (R6G) molecules. The emission of the layer was excited by a laser diode with the 532-nm central wavelength under the fixed irradiation angle, θ^{in}, of 67° to the surface normal. The linearly-polarized pump radiation scattered from the nanostructure and collected by a lens was completely blocked using appropriate long-wavelength pass filters placed in front of the CCD-camera in the microscope and providing attenuation of the pump radiation about ~10^6. For large-area PL imaging the CCD-camera and the lens with NA=0.6 were used, while for PL mapping a home-build confocal scheme, including a high-NA lens (100x, NA=0.9), a multi-mode optical fiber, acting as a pinhole, and an avalanche photodetector were used. The enhancement coefficient EF_{PL} was estimated as a ratio of the PL intensity I_{sig} measured from the film area, containing the single nanovoid or the patterned area, to the PL intensity I_{surf} measured from the flat film surface of the same square. SERS spectra from the R6G layer were acquired using a micro-Raman spectrometer (HORIBA LabRam HR, AIST SmartSPM) and a 2-mW, 632.8-nm He-Ne pump laser, being collected by a set of a 100× microscope objective (NA=0.9), a 600-g/mm diffraction grating and a thermoelectrically cooled CCD-array (Andor DU 420A-OE 325). Separate spectra were recorded at 0.5-mW pump power for both such spots, and from a 1-cm wide cuvette of neat R6G solution for normalization. From these measurements, the SERS enhancement factor EF^{SERS} averaged over the excitation beam size, was estimated as $EF^{SERS} = (I_{SERS}/I_{norm})(N_{norm}/N_{SERS})$, where I_{SERS}, I_{norm} and N_{SERS}, N_{norm}, are the intensities and the numbers of the probed molecules on the sample and on the reference surface at specific Raman bands (615 and 1364 cm^{-1}), respectively.

To probe plasmonic enhancement in the near-UV spectral region, silver nanovoids were covered by a 10-nm thick layer of Eu^{3+}(TTA) [an alkylated europium complex, tris(α-thenoyltrifluoroacetone)(1-octadecyl-2(-2-pyridyl) benzimidazole) europium(III)] and their PL intensity enhancement was measured. Detailed description of Eu^{3+}(TTA) synthesis and its optical properties are presented in *Supplementary information* (Note 1).

Calculations of metal distribution along the nanovoid shell. To simulate complicated three-dimensional flows with melting and crystallization phase transitions we have utilized a combination of

Nanoscale Accepted Manuscript

This journal is © The Royal Society of Chemistry 2016

Please do not adjust margins
View Article Online
DOI: 10.1039/C6NR01317A

Published on 10 May 2016. Downloaded by Middle East Technical University (Orta Dogu Teknik U) on 10/05/2016 10:26:07.

numerical and theoretical techniques. Two-temperature hydrodynamic (2T-HD) code was used to simulate motion at the early stages. These stages include (i) absorption of a femtosecond pulse during ~200 fs, (ii) heating of electrons in a skin layer during the pulse, (iii) fast spreading of the absorbed energy from a 15-nm thick skin layer into a 50-nm thick metal film and homogenization of the electron temperature T_e across the film thickness (1-2 ps), melting on a picoseconds time scale, (iv) electron-ion temperature relaxation (5-7 ps) and (v) hydrodynamic interaction between the film and the substrate. During this interaction the film as whole accumulates a momentum which later leads to separation of a film from the substrate. Further details concerning the 2T-HD calculation are presented in [29,30]. From these 2T-HD calculations we have derived the dependence of separation velocity $v_{sep}(r)$ on the absorbed fluence. This velocity distribution has a maximum value on the axis of the laser beam (r=0). Thus, three-dimensional cupola-like shape of the separated film is gradually developing during its lift-off. Such three-dimensional evolution of nanovoid cupola were described using a molecular dynamics (MD) code [31] with a Monte-Carlo (MC) solver added to simulate heat-conduction cooling and freezing of the nanovoid. In the simulations, electron jumps from a host atom to its neighbor, resulting in heat transport from hot to cold regions in the electron gas, were considered. The thermal diffusion coefficients χ_{1T}, used in the simulations, were adjusted to the necessary value, varying the frequency of electron jumps per electron v_D, the electron-ion collisional frequency v_{ei} and the effective electron mass m_{eff}. During the simulation run, in the periphery region the temperature T_{th} below the melting temperature of gold T_{th} < 1337 K is supported by a thermostat localized in the periphery area, covering the region between the simulation box L_bxL_b and the circle r = L_b-2Δ. The following parameters were used for MD+MC simulations: the metal film thickness d=10 nm, Δ=5 nm, L_b=270 nm, the heat conduction coefficient κ=42 $Wm^{-1}K^{-1}$, the surface tension value σ=540 dyn/cm. Two main dimensionless parameters, governing the flow, are the capillary and thermal numbers

$$v_{0\sigma}=v_{sep}(r=0)/v_\sigma \text{ and } v_{0\chi}=v_{sep}(r=0)/v_\chi$$

where $v_\sigma=2\sqrt{(\sigma/\rho_0 d)}$, $v_\chi=2\chi/D$ is the cooling velocity, χ – thermal diffusivity, ρ_0 – initial density, d – metal film thickness, D – diameter of the nanovoid base. The initial velocity profile v ~ $\cos^2$ was considered. The thermostat supports the temperature T_{th} and does not allow the film to separate from the substrate in the periphery region. Thus, the condition of cohesive binding of the film to the substrate outside the cupola is fulfilled. The momentum of the flying cupola is gradually transmitted to the substrate through surface tension in the molten region of the film, through the tensile stress, preventing stretching in surrounding solid film, and finally by the cohesion to the substrate. This set of stresses decelerates the motion of the cupola at the stage, when the cupola lifts-off from the substrate. Thin-shell model [29,30] was used to calculate the mass distribution inside the nanovoid shell (cupola) by adjusting the values of the capillary number as well as the velocity radial distributions to fit the experimentally measured external dimensions of the nanovoids. Combined 2T-HD-MD-MC calculations were performed on the "Lomonosov" supercomputer at Moscow State University.

Numerical simulations of the optical properties. Scattering spectra and corresponding EM near-field distributions were calculated, using a commercial FDTD solver (Lumerical Solutions). The external (visible) dimensions of the hollow nanovoids were given by AFM measurements, while the inner material distributions including the thickness of their shells as well as the distribution and the amount of the material near its tip were provided by the results of the MD+MC simulations. The nanovoids were obliquely illuminated (at an angle of 63° from the surface normal) by the total-field scattered-field source, while tabulated spectra of dielectric functions for Au, Ag and quartz [32] without top oxide layer were considered. Two-dimensional case was considered, assuming that the nanovoids have their infinite length along z-axis (Fig.4A). The elementary Yee cell size was as small as 0.1x0.1 nm^2, ensuring elimination of the stair-case effect, when modeling highly curved surfaces with square-shaped cells. Back-scattering spectra were collected by the two-dimensional detector with the aperture equal to the aperture of the lens used in our experiments.

Results and discussions

Fabrication and geometric shape fitting of the nanovoids. A series of side-view SEM images (Fig.2(A-H)) illustrates the results of single-pulse nanoablation of the 50-nm thick Au film on the bulk glass substrate. As seen, the irradiation of the metal film by the tightly focused fs-laser pulse results in formation of an extremely-small submicron-sized parabolic-shaped nanovoid at the interface between the film and the substrate, which external size increases versus *E*, eventually taking the fully conical shape at E≥1.7 nJ (Fig.2(D-E)). At the further increase of the pulse energy an elongated jet-like tip appears at the upper part of the nanovoid [26], driven by the increased accumulation of the molten material (Fig.2(F-H)). Finally, when the pulse energy exceeds some critical value the thinned nanovoid shell breaks (Fig. 2(H)), resulting in ejection of the central nanojet and formation of the through microhole (not shown). Owing to the sharp focusing of the laser pulse on the metal film surface, the formation and subsequent destruction of the nanojet occurs without formation of a counter-jet [30,33-36].

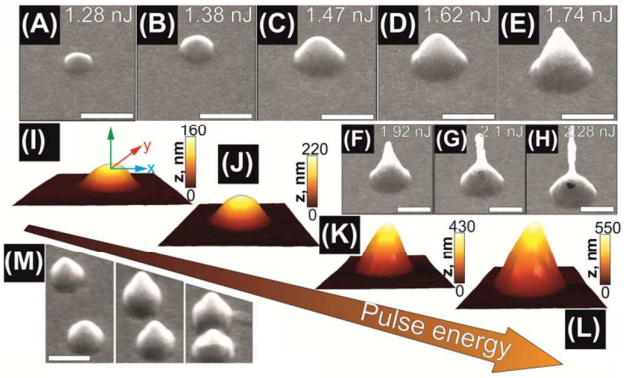

Fig.2. Fabrication of gold nanovoids. (A-H) Side-view SEM images (at an angle of 45°) of the Au nanovoids fabricated by single fs-pulse irradiation of the 50-nm thick gold film on the glass substrate at the increasing pulse energy E. (I-L) AFM images of the nanovoids shown in (A-D). (M) Series of side-view (at an angle of 45°) SEM images of nanovoid pairs with different inter-distances of 1.2, 0.72 and 0.5 μm (from left to right).The scale bar in all SEM images corresponds to 500 nm.

The geometric shape of the fabricated nanovoids can be characterized by the maximal height *h* measured from the initial level of the metal film (inset in Fig.3A), the nanovoid base diameter

Nanoscale Accepted Manuscript

Please do not adjust margins

View Article Online
DOI: 10.1039/C6NR01317A

Published on 10 May 2016. Downloaded by Middle East Technical University (Orta Dogu Teknik U) on 10/05/2016 10:26:07.

D, the circumference *L*, and the curvature radius R_{tip} of its tip. Since the exact values *h* and R_{tip} can't be accurately measured at the oblique angles of the SEM inspection, such measurements were done by AFM scanning. Figures 2(I-L) demonstrate a series of AFM images of the nanovoids previously depicted in Fig. 2(A-D), showing the growth of their dimensions – their height increases from 160 to 550 nm and their diameter increases from 420 to 700 nm, while the curvature radius demonstrates some changes only when the nanojet formation takes place. Such increase of the nanovoid size – both diameter and height – leads to its reshaping from the parabolic (Fig.2A-C) to the quasi-conical profile (Fig.2D-F), which will be discussed below in detail.

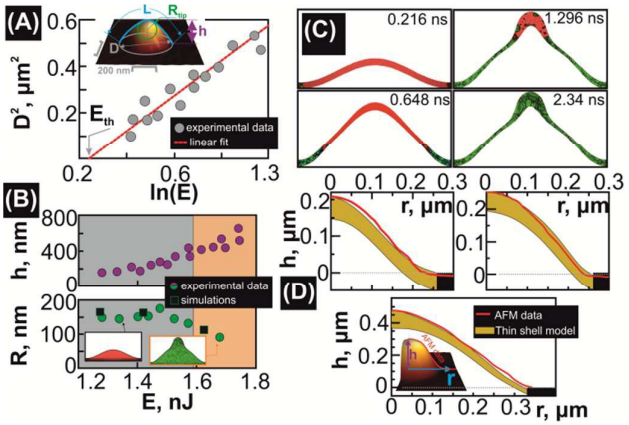

Fig.3. Geometric shape and dimensional fitting of gold nanovoids. (A) Squared diameter D^2 of the nanovoids versus natural logarithm of the pulse energy ln(E) (in nanojoules). The linear fit of this dependence indicates the characteristic Gaussian diameter $D_{1/e}$ = 1.13 μm of the surface energy distribution as well as the threshold formation energy for hollow nanovoids; (B) Height of the nanovoids h and curvature radius of its tip R_{tip} versus the pulse energy E. Two insets illustrate the parabolic- and conical-shaped nanovoids both simulated with the developed MD+MC approach. (C) Time evolution of the nanovoid shell according to the MD+MC simulation. For this simulation the following values are used: $v_{sep}(r=0)$=200 m/s, v_{σ}=106 m/s, $v_{0\sigma}$=1.9, v_{χ}=130 m/s, $v_{0\chi}$=1.5. Green color corresponds to the resolidified gold, while red color – to its liquid phase. (D) Metal distribution along the shell of the parabolic-shaped nanovoids simulated, using the thin-shell model. The upper boundaries of the nanovoid shells measured by AFM (red solid curves) are presented in all images for comparison. AFM data were obtained by averaging at least 20 surface profiles of the similar nanovoids.

As can be seen, the shape as well as the main geometric parameters of the nanovoids systematically presented in Figs. 3(A,B), can be fitted well as functions of the input pulse energy E. The characteristic Gaussian diameter of the surface energy distribution $D_{1/e}$ extracted via the slope of the line [37] fitting the dependence D^2- ln*E* was found to be equal to 1.13 ± 0.07 μm (see. Fig. 3A). This value substantially exceeds both the Au film thickness and the optical spot radius R_{opt} ~ 0.34 μm, indicating the significant lateral heat transfer. This dependence also indicate the threshold energy E_{th} (Fig. 3(A)) and the threshold fluence F_{th} required for nanovoid formation, which are equal to $E_{th,Au}$ ≈1.23 nJ and $F_{th,Au} = E_{th}/\pi(R_{1/e})^2$ = 0.11±0.02 Jcm^{-2}, respectively. ‡For the relatively high absorbance of the 50-nm-thick Au film, A=0.152 at λ=532 nm [32], the threshold absorbed fluence is $F_{ab,Au}$ = 0.017±0.001 $mJcm^{-2}$ in reasonable agreement with the previously published results [33,38].

Note that the combination of tilted SEM imaging and AFM scanning provides rather accurate way to measure the outer dimensions of the nanovoids, while giving practically no information regarding the inner material distribution inside the nanovoid shell. To give insight into the inner material distribution in the cupola shells, numerical simulations were performed using the hybrid 2T-HD-MD-MC theoretical approach (see *Experimental* section and *Supplementary information* for more details). Fig. 3C illustrates the temporal evolution of the nanovoid shell produced in the 10-nm thick Au film till its complete freezing calculated using MD-MC simulations. These qualitative snapshots exhibit significant material redistribution from the nanovoid periphery toward its tip as well as the appearance of the additional inflection points in the shell when the nanovoid acquire the conical shape, while for the parabolic-shaped nanovoids the material redistribution along the nanovoid circumference is negligible. Meanwhile, comparing to the calculation in experiments we have 5-fold thicker metal film as well as higher values of solidification velocity v_{χ}= 480 m/s and surface tension σ=100 dyn/cm (see *Experimental* section). Thus, to describe the results MD+MC calculations and to directly compare these findings with the experimentally measured nanovoid topography we have used thin-shell model [30,31]. The results of material redistribution along the nanovoid shells with variable dimensions are presented in Fig.3D. As can be seen, the results of the thin-shell modeling show good quantitative agreement with the "visible" geometrical dimensions of the parabolic-shaped nanovoids accurately measured using the AFM scanning (red solid curves) in terms of both the curvature radius R_{tip} (see also Fig.3B) and the surface profile, determining the diameter D and height h of the nanovoids. Some deviations from the AFM profiles near the nanovoid base are associated with the sophisticated physical picture of the metal film separation from the substrate including cohesion, resistance of a solid film to mechanical bending and pre-melting. More importantly, these results also show that for the parabolic-shaped nanovoids of small and mean heights the thickness deviations along the circumference L are quite small (the tip area has the thickness of 59 nm, which is only 20-% thicker than the initial film, Fig.3D), as was qualitatively predicted by the MD+MC simulations. For the highest parabolic-shaped nanovoid (h=420 nm, D=630 nm), which require the pulse energy E~1.6 nJ close to the nanovoid reshaping threshold (Fig.3B), the thin-shell model estimates 2-fold thickening of the tip area, as compared with the initial film thickness, indicating the initiation of the nanojet formation in good agreement with our experimental findings. Similar conical microstructures were fabricated by irradiating the 50-nm-thick Ag film on the glass substrate under the same experimental conditions. However, when the Ag microstructure reaches some critical dimensions, we have observed the formation of multiple cracks in the cupola walls, appearing mainly near the nanovoids base (for details see Note 3 *Supplementary information*). Apparently, this process governs the destruction of the nanovoids prior to formation of the elongated nanojet in the upper part of the nanovoids. Such behavior can be explained by lower surface tension of molten silver (0.9 N/m [39]), comparing to that of molten gold (1.13 N/m). Lower plasticity and higher melting temperature [40] of silver in comparison to those of gold can be also the reasons for the crack formation in the Ag nanovoids. In the case of silver, its dependences of *h* and R_{tip} on the pulse energy demonstrate the same trends (not shown here), as similar dependences of the Au nanovoids. In contrast, formation of nanovoids is less sensitive to thermal conductivity of film substrate (see Note 4 in *Supplementary information*). Importantly, spatial separation between adjacent hollow nanovoids can be even

Nanoscale Accepted Manuscript

This journal is © The Royal Society of Chemistry 2016

Please do not adjust margins
View Article Online
DOI: 10.1039/C6NR01317A

smaller, than 500 nm (see Fig. 2M), being compared with a laser-induced forward transfer technique [41-43], where typical separation between transferred droplets equals to 1-2 μm.

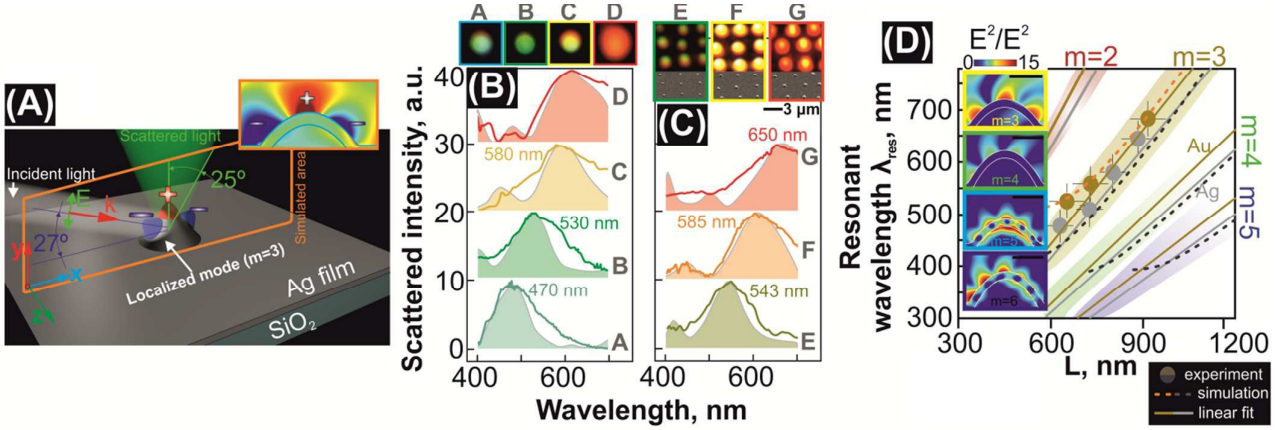

Fig.4. Scattering properties of noble-metal parabolic–shaped nanovoids. (A) Sketch schematically illustrating the origin of the resonant single-color scattering and geometry simulated using the finite-difference time-domain calculation; (B) Experimentally measured (solid curves) and calculated (dashed curves) normalized back-scattering spectra from the individual Ag nanovoids (marked by "A","B","C","D" letters) and (C) small arrays of Au nanovoids (marked by "E", "F", "G" letters). Reference SEM and correspondent dark-field images are also given in the insets. All spectra were normalized and vertically off-set by 10 a.u. for clarity. All experimental spectra were averaged over at least 20 measurements of the identical structures. (D) Calculated (solid curve), experimentally measured (circles) and numerically simulated (dashed curves) maximum scattering wavelength versus the nanovoid circumference length L for the Au and Ag nanovoids. The insets show typical normalized squared E-field amplitude $|E|^2/|E_0^2|$ distributions near the Ag parabolic-shaped nanovoids for transverse mode numbers m=3,4,5,6, calculated under appropriate resonant excitation, with the incident field excluded for clarity.

More importantly, cost-effective single-shot laser fabrication of plasmonic nanovoids based on rapid melting, deformation and resolidification of the noble metal films provides the highly controllable way to produce separate nanovoids and their ordered arrays with very smooth walls (according to AFM measurements with 5-fold lower roughness), being advantageous in comparison with other fabrication techniques based, for example, on thermal deposition of metal onto nanotextured templates (see, for example, [3,8,16]).

Plasmonic properties of noble metal nanovoids. Using the abovementioned fabrication approach, the surface of the 50-nm thick Ag film on the glass substrate was patterned in the form of a large-scale well-ordered array of different-shaped nanovoids (see *Supplementary information,* Note 5). The distance between the neighboring nanovoids was set to 2 μm, which is far enough to collect scattered light from each individual nanoelement. Surprisingly, some individual parabolic-shaped nanovoids demonstrate single-color resonant light scattering in the visible spectral range under oblique illumination by unpolarized white light in the dark-field scheme (Fig. 4A).

This resonant scattering is clearly observed both in the dark-field optical images appearing for some individual nanostructures as bright single-color spots (insets in Figs.4B,C) and by direct measurements of the back-scattering spectra directly collected from the individual nanovoids (Fig.4B,C). More importantly, the spectral position of the scattering peak distinctly red-shifts with the increase of the nanovoid size. As can be seen from the series of scattering spectra measured from the single silver nanovoids (Fig. 4B), the main scattering peak shifts from 470 to 615 nm, while the height h of the nanovoid increases from 160 to 320 nm and its diameter – from 420 to 580 nm. Similar situation takes place for gold nanovoids, where the evident size-dependent redshift of the scattering peak from 543 to 650 nm is observed as the size of the nanovoid increases (Fig. 4C). Apparently, the observed far-field resonant light scattering from such individual nanovoids can be attributed to the excitation of the different localized or even delocalized plasmon modes. However, typical separation of 2-3 μm between neighboring nanovoids in our experiments completely excludes the contribution of delocalized plasmon modes in the visible spectral range. Considering in details the laser-induced formation process of the nanovoids, several major features, potentially affecting the excitation of plasmon modes, can be highlighted and discussed. First, fast separation of the metal film from the glass substrate produces highly curved surfaces near the nanovoid base and tip, which can become the places where the plasmon wave can be efficiently excited, reflected or scattered. The curvature near the base increases with nanovoid dimensions, likewise the reshaping of the nanovoid cupola from parabolic to quasi-conical produces both uneven material distribution along the nanovoid shell and additional inflected point which can potentially influence the process of plasmon excitation and propagation. Second, increase of the nanovoid dimensions also yields in redistribution and accumulation of the molten film from the periphery toward the center of the nanovoid. For highly-pitched nanovoids (see Fig.2I-J) with relatively large amount of accumulated material near the nanovoid tip, its central part actually can act as a separate nanoantenna. Such specific material distribution inside the nanovoid was underlined and discussed in the previous section in terms of MD modeling and is also particularly confirmed by SEM images (see Figs. 2 and 3), where the upper part of the nanovoids appears in bright color, indicating stronger secondary electron emission, while the thicker wall near the cone base looks even darker, than the unmodified metal film. For this reason, highly-pitched conical-shaped nanovoids (see Supplementary information, Note 5) emit predominantly as bright yellow-red multi-color spots and their scattering spectra demonstrate no pronounced resonant size-dependent features. Hence, we will limit our study below by the optical properties of the parabolic shaped nanovoids.

Published on 10 May 2016. Downloaded by Middle East Technical University (Orta Dogu Teknik U) on 10/05/2016 10:26:07.
Nanoscale Accepted Manuscript

Please do not adjust margins

View Article Online
DOI: 10.1039/C6NR01317A

Published on 10 May 2016. Downloaded by Middle East Technical University (Orta Dogu Teknik U) on 10/05/2016 10:26:07.

Under oblique irradiation with unpolarized light, metal nanovoid as typical reduced-symmetry nanostructure can support both axial and transverse types of localized plasmon modes [44]. The axial modes were shown to produce scattering signal directed far away from normal direction under oblique excitation [44]. In this relation, such modes should contribute slightly to the measured back-scattering spectra, considering the finite numerical aperture of the lens used to collect the scattering signal. Transverse modes were shown to be well defined by the standing-plasmon-wave model [3], suggesting the simple resonance conditions

$$Ln_{eff}=m\lambda_{res}/2,$$

where the effective refractive index of the plasmon wave supported by the film-vacuum interface $n_{eff}=\sqrt{\varepsilon_m(\lambda)(\varepsilon_m(\lambda)+1)^{-1}}$, ε_m is the spectrally-dependent dielectric permittivity of the metal, λ_{res} is the resonant wavelength of the scattered light, m is the integer number corresponding to the number of plasmon half-wavelengths, that fits the circumference of the nanovoid L. The value L can be roughly defined in terms of the previously presented geometric parameters as $L\approx\sqrt{(h-R_{tip})^2+(0.5D-R_{tip})^2}+\pi R_{tip}$, in its turn. Surprisingly, the experimentally measured dependence of the maximum scattering position for such Au and Ag nanovoids shows almost linear dependence versus L (Fig. 4D) and coincides well with the linear fit for the odd plasmon mode with m=3 (for details, see the *Supplementary information,* Note 6). This indicates the pure geometric origin of the observed resonant wavelength shift and the predominant contribution of this mode to the observed single-color far-field scattering.

To reveal the origin of the observed resonant light scattering from the individual nanovoids in the visible spectral range and to relate these resonances to both structural features and certain plasmon mode types, FDTD calculations were undertaken. The outer dimensions of the hollow nanovoids were provided by the AFM measurements, while the inner material distributions including the thickness of the nanovoid shells as well as the distribution and the amount of the material near its tip were extracted from the results obtained using abovementioned thin shell approximation. In our model we have considered 2D case suggesting the infinite size of the nanovoid along z-axis and its oblique illumination (at an angle of 63°) with p-polarized light. Under such circumstances the only transverse plasmonic modes will be excited, scattered and collected by the two-dimensional monitor with the size coinciding with the experimental NA of the lens (Fig. 4A).

The calculated scattering spectra from the individual Ag and Au nanovoids (dashed curves in Fig.4B,C) of variable size demonstrate satisfactorily good agreement with the experimentally measured spectra, exhibiting good coincidence of the resonance spectral positions versus the circumference of the nanovoid L (dashed curves in Fig.4D). The characteristic normalized squared electric-field amplitude $|E|^2/|E_0|^2$ near the Ag nanovoids with various geometric sizes (see the upper inset in Fig. 4D and *Supplementary information, Note 7*), calculated at the corresponding resonant wavelength, have similar structure in all considered cases, indicating the common nature of the resonant light scattering in the visible spectral range and confirming the "geometric" origin of the resonance shift. As can be seen from these distributions, the enhanced electromagnetic spots are located near the cupola walls coinciding with m=3 transverse plasmon mode, which fits 3 half-wavelength along the nanovoid circumference L. Such transverse plasmon mode is governed by the excitation and effective scattering of the surface plasmon waves localized between two highly-curved sections near the void base, both on their outer and inner sides. Additional resonant features clearly identified in the calculated spectra for Ag nanovoids and blue-shifted from the main scattering peak (Fig. 4B) can be attributed to excitation of higher-order (m=4 and 5) plasmonic modes. For such modes the calculation also gives good agreement with the linear standing-wave approximation (see Fig. 4D). Similarly, for Au nanovoids (Fig. 4C), the appearance of the additional features in the calculated spectrum near 500 nm can also attributed to high-order mode excitation, while the features near 400 nm is apparently associated with some approximations during the calculation – e.g., one caused by a fitting procedure for the experimental gold spectrum [32]. Likewise, in the experimentally measured DF spectra both for Ag and Au nanovoids (Fig. 4B,C) these features can hardly be identified apparently owing to the low efficiency of the white-light source in this spectral region, as well as the increase of the spectral maximum broadening with its red shift. Importantly, for the finite numerical aperture, providing full collection angle of 50°, the contribution of plasmon modes with odd m numbers (i.e., m=3,5) to the back-scattering spectrum is significantly higher, than for even-number modes. This particularly can be explained in terms of the characteristic-field distribution for odd modes with their maximal field intensities coinciding with the nanovoid tip (insets in Fig. 4D), which acts as an efficient scatterer of the plasmon waves, in turn. Finally, considering the relatively approximate character of these calculations, they give satisfactorily good predictions of resonant peak position versus nanovoid circumference. However, the overall picture revealing all types of modes excited in the nanovoids as well as their contributions can require more complicated analysis, including collection angle- [44] and polarization-resolved [8] studies of the back-scattering spectra, supported by comprehensive three-dimensional numerical simulations. Additional processes, including excitation and energy exchange between plasmon modes excited on the outer and inner sides of the nanovoid, hybridization of the and localized plasmons of the nanovoid and delocalized ones supported by the metal film, as well as other relevant physical phenomena [8,44-46], should be also considered.

Biosensing applications of plasmonic nanovoids. Spontaneous emission from quantum nanoemitters is known to be significantly increased or quenched [47,48] near hot spots, produced by plasmonic nanostructures. In order to probe the presence of such plasmon-mediated electromagnetic fields near the hollow nanovoids, as well as to demonstrate some biosensing capabilities of such structures, the fabricated silver nanovoids were covered by a thin layer of R6G molecules. Figure 5A shows a PL map (see *Experimental* section for details) of the 10-nm-thick R6G layer, covering a small array of silver nanovoids tuned to provide maximum E-field enhancement near the PL excitation wavelength λ=532 nm. This PL image clearly indicates the substantially enhanced signal from the R6G layer near the nanovoids apparently associated with intense electromagnetic near-fields close to their walls, originating from the excitation of the SPP-modes. A series of images in Fig. 5B presents a large-scale complex-shaped array (with up to 10^3 elements) of the Ag nanovoids fabricated at 100-Hz pulse rate and fast scanning (500 μm/s) rate demonstrating the applicability of the fabrication technique for large-scale pattering. By measuring the R6G emission spectra from the small area (approx. 0.8 μm^2), containing a single nanovoid, and comparing it with those from the area of the same size on the smooth silver film, at least 6-fold enhancement of the PL signal was observed (Fig. 5C). Additionally, both measured emission spectra have the same

Nanoscale Accepted Manuscript

This journal is © The Royal Society of Chemistry 2016

Please do not adjust margins
View Article Online
DOI: 10.1039/C6NR01317A

Published on 10 May 2016. Downloaded by Middle East Technical University (Orta Dogu Teknik U) on 10/05/2016 10:26:07.

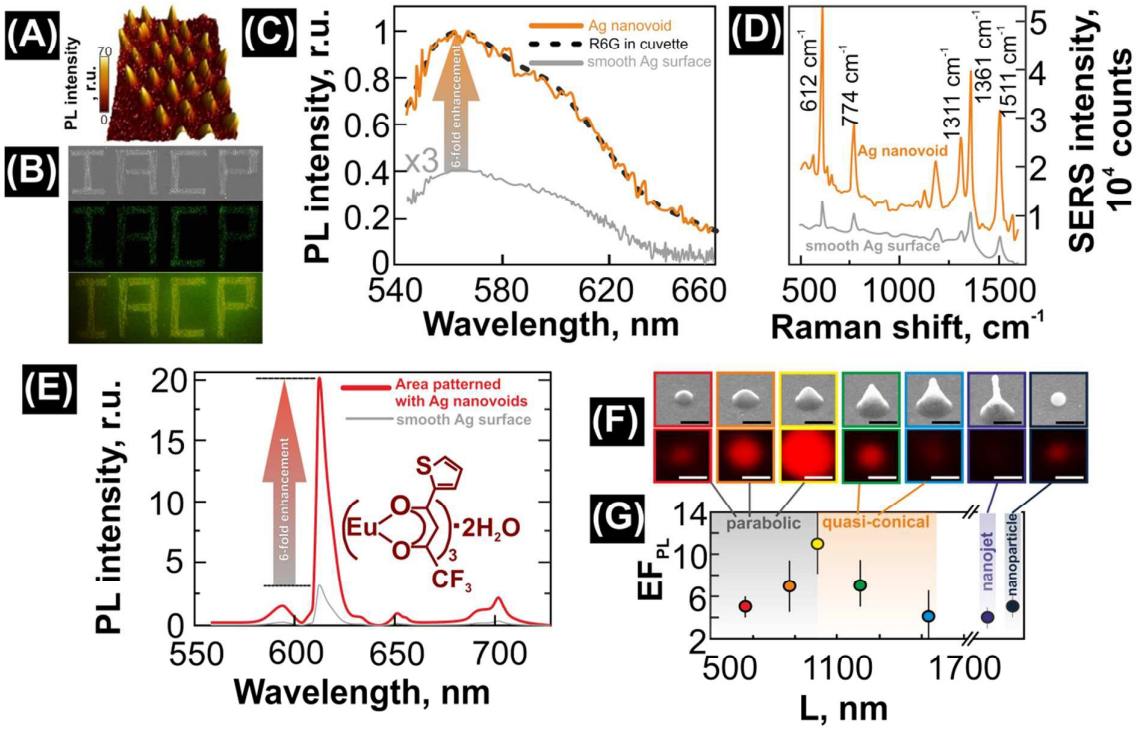

Fig. 5. Surface-enhanced PL and Raman scattering of the nanoemitters covering silver nanovoids. (A) PL map of the R6G layer on the Ag hollow nanovoid array, showing enhanced signal coming from emitters placed in the vicinity of nanostructures. The distance between the adjacent nanovoids is 3 μm. The averaged background was subtracted from this map for better displaying; (B) Reference side-view SEM (top), optical (middle) and PL (bottom) images of the area patterned with Ag nanovoids arranged into "IACP" letters and covered with 10-nm thick R6G layer; (C) Normalized PL spectra of the R6G measured on the single Ag nanovoid (orange), smooth 50-nm thick Ag film (grey), and from the alcoholic solution in cuvette. The signal from the R6G layer on smooth silver film was magnified by 3 for better displaying shape of the emission spectrum; (D) Comparison of R6G Raman spectra measured on the smooth Ag film surface (grey) and on single crack-free nanovoid (orange); (E) Averaged Eu^{3+}(TTA) PL spectra measured from the patterned area (approx. 5x25 μm^2) containing various nanovoids in comparison with PL spectra measured from smooth Ag film of the same size; (F) Series of SEM and PL image pairs illustrating the size- and shape-dependent enhancement of the PL signal from the Eu^{3+}(TTA) layer covered the silver nanovoids. Last pair of images illustrates the PL signal enhancement from the 250-nm-wide spherical Ag nanoparticle; (G) PL enhancement factor EF_{PL} versus the L.

appearance, as the emission spectrum measured for the R6G solution in ethanol (dashed curve in Fig.5C).

This clearly indicates that the plasmon-mediated enhancement of electromagnetic fields near the nanovoids, which increases the spontaneous emission of R6G molecules, is the main mechanism responsible for the observed PL signal enhancement [47]. In contrast, the contribution of the plasmon-coupled emission, which can significantly reshape the emission spectrum of the molecules, is relatively small in this case [48]. SERS spectrum of the R6G layer (Fig. 5C), covering a single parabolic-shaped silver nanovoid, demonstrates spatially averaged enhancement factor $EF_{void} \sim 5 \cdot 10^4$ (for SERS measurement details and estimations see *Experimental* section and *Supplementary information*, Note 2).

Finally, low UV emission efficiency of our white-light source used for DF scattering experiments, significantly complicates probing high-order plasmonic modes with resonant wavelengths lower than 450 nm. To probe the presence of such modes as well as biosensing capabilities of the silver nanovoids in the near-UV spectral region, an array of nanovoids with various shapes and sizes (*Supplementary information,* Note 8) was covered by a 10-nm thick layer of Eu^{3+}(TTA), providing very stable emission at λ=612 nm (the main emission line) under UV-light excitation [49,50] (for details see *Experimental* section and *Supplementary information,* Note 1).

Additionally, near the nanovoid-patterned area we have also produced 1-μm wide through holes with plurality of sharp resolidified features and spherical nanoparticles around the craters using multi-pulse irradiation. Surprisingly, either these features or the highly-pitched conically shaped nanovoids (marked with purple and blue circles in the Fig.6(e), respectively) provide low PL signal enhancement, being compared with enhanced emission from the Eu^{3+}(TTA) nanoemitters located near the parabolic-shaped nanovoids of even smaller size (see Fig. 5F). The presented area (approx. 5x25 μm^2) patterned with the Ag nanovoids was shown to produce 6-fold average enhancement of all four Eu^{3+}(TTA) emission lines (Fig.5E), as compared with the smooth Ag film of the same size. Likewise, the PL enhancement factor EF_{PL} for individual parabolic-shaped nanovoids (approx. 0.8 μm^2) was as high as 13 times (Fig.5G).

Lower PL signals from conical-shaped nanovoids and nanojets, comparing to parabolic-shaped nanovoids, are apparently

Nanoscale Accepted Manuscript

Please do not adjust margins

View Article Online
DOI: 10.1039/C6NR01317A

Published on 10 May 2016. Downloaded by Middle East Technical University (Orta Dogu Teknik U) on 10/05/2016 10:26:07.

associated with lower local E-field amplitudes, resulting from the strong scattering of the high-order plasmon modes. Significantly lower curvature radius R_{tip} of the conical-shaped nanovoid tip, uneven material distribution, additional inflection points (see *Supplementary information,* Note 8), as well as higher nanovoid circumferences *L* supporting higher mode numbers *m*, can be the reasonable arguments, describing the lower E-field amplitudes for conical-shaped nanovoids. Considering the minimal possible area of 0.8 μm^2 for the PL signal accumulation, the presented parabolic-shaped nanovoids (first 3 pairs in Fig.5F) produce approximately the same EF_{PL} value normalized on the nanovoid size. Finally, the parabolic-shaped nanovoids demonstrate PL enhancement, comparable to that of a 250-nm wide Ag nanoparticle (last pair in Fig.5F) produced by laser-induced forward transfer technique, also indicating good applicability of the fabricated nanovoids for biosensing purposes.

Conclusions and outlook

In conclusion, resonant light scattering from individual hollow nanovoids fabricated by single-pulse laser nanoablation of thin supported noble metal films on glass substrates was observed for the first time, using dark-field confocal microspectroscopy. The spectral positions of the resonant scattering peaks in the visible spectral range were found to be fully determined by the nanovoid size. These colored geometric resonances were attributed to excitation and efficient scattering of high-order transverse plasmon modes in the shells of the nanovoids. This hypothesis was proved by means of the comprehensive computational approach, which includes the Two-Temperature Hydrodynamic Molecular-Dynamic Monte-Carlo modeling of the material distribution inside the hollow nanovoids and subsequent finite-difference time-domain EM calculations exploiting the simulated nanovoid shapes. The averaged 6-fold enhancement of the PL signal from both the layers of alkylated europium complex salts embedded into the organic matrix and common Rhodamine 6G molecules was experimentally demonstrated. Additionally, the individual silver nanovoids show the spatially averaged enhancement of the R6G Raman signal by $5 \cdot 10^4$ times, as well as the shape- and size-dependent PL enhancement as high as 13 times for specific individual nanostructures. The presented cost-effective technique of fabrication of hollow noble-metal nanovoids can be useful for metal coloration, high-performance and cheap printing of functional ordered substrates for plasmonics, field-emission devices, solar cells, biosensing, etc. More generally, the presented cost-effective laser-assisted printing based on rapid melting, deformation and resolidification of thin noble-metal films provides the highly controllable way to produce the separate nanovoids and their ordered arrays with very smooth walls, as compared with other fabrication techniques based on thermal metal deposition onto nanotextured templates (see, for example, [3,8,16]). However, the formation process of such noble-metal nanovoids for high-NA focusing lens occurs in very narrow range of pulse energies, implying usage of very stable lasers to fabricate relatively large arrays with small geometric size deviations for each nanoelement to provide their identical plasmon-resonance spectral position. In this respect, we suppose that single-pulse interference (3- or 4-beam, [2]) lithography as well as utilization of microlens arrays and masks [51,52], in which pulse-to-pulse energy fluctuations are completely eliminated, will be beneficial for fast high-repetition-rate laser fabrication of highly-ordered arrays of such hollow nanovoids. Finally, here we have demonstrated the plasmonic nanovoid formation with tunable geometric parameters, using both the fixed numerical aperture of the focusing lens (NA=0.95) and the fixed thickness of the metal film. Likewise, it is obvious that utilization of lower NA values and thicker (thinner) films will provide additional possibility to tune shape as well as height-to-diameter ratio of such printed nanovoids.

Acknowledgements

Authors thanks Dr. A. Zhizchenko and Dr. A. Dysliuk for helpful discussions. Authors from IACP and FEFU are grateful for partial support to the Russian Foundation for Basic Research (Projects nos. 15-02-03173-a, 15-02-08810-a, 14-29-07203 ofi_m, 16-38-60184_dk) and the "Far East" Program of FASO. A.A. Kuchmizhak is acknowledging for partial support from RF Ministry of Science and Education (Contract No. MK-3056.2015.2) through the Grant of RF President. This work was also supported by the RAS Presidium program and the Government of the Russian Federation (Grant 074-U01) through ITMO Visiting Professorship Program for S.I. Kudryashov. Molecular dynamic simulations and lateral heat transfer estimations were financially supported by the grant 14-19-01599 of Russian Science Foundation.

Notes and references

‡Absorption of a part of laser energy takes place in a skin layer of the thickness $\delta_{sk} = \lambda/4\pi k = 20.1$ nm, where $n + ik = 0.384 + 2.11i$ and $\varepsilon_1 + i\,\varepsilon_2 = -4.3 + 1.62i$ are refraction index and dielectric constant of gold at $\lambda = 532$ nm, respectively. Reflectance for the normal incidence is $R = 0.765$; transmittance through the 50-nm thick film is approximately $e^{(-50/20.1)} = 0.083$. Thus, the absorbance of the film is $A = 1 - 0.765 - 0.083 = 0.152$.

1 J. Liu, A.I. Maaroof, L. Wieczorek, M.B. Cortie, *Adv. Mat.*,2005, **17**, 1276.
2 J.C. Love, B.D. Gates, D.B. Wolfe, K.E. Paul, G.M. Whitesides,. *Nano Lett*., 2002, **2**, 891.
3 T.A. Kelf, Y. Sugawara, R.M. Cole, J.J. Baumberg, M.E. Abdelsalam, S. Cintra, P.N. Bartlett,. *Phys. Rev. B*, 2006, **74**, 245415.
4 H. Takei, M. Himmelhaus, T. Okamoto, *Opt. Lett.*, 2002, **27**, 342.
5 C. Charnay, A. Lee, S.Q. Man, C.E. Moran, C. Radloff, R.K. Bradley, N.J. Halas, *J. Phys. Chem. B*, 2003, **107**, 7327.
6 T.V. Teperik, F.G. De Abajo, A.G. Borisov, M. Abdelsalam, P.N. Bartlett, Y. Sugawara, J.J. Baumberg, *Nat. Photon*., 2008, **2**, 299.
7 N.A. Mirin, N.J. Halas, *Nano Lett*. 2009, **9**, 1255.
8 Y. Zhang , A. Barhoumi, J.B. Lassiter, N.J. Halas, *Nano Lett.*, 2011, **11**, 1838.
9 D.O. Sigle, E. Perkins, J.J. Baumberg, S.J. Mahajan, *Phys. Chem. Lett.*, 2013, **4**, 1449.
10 N.M. Perney, F.G. García de Abajo, J.J. Baumberg, A. Tang, M. Netti, M.D. Charlton, M.E. Zoorob. *Phys. Rev. B*, 2007, **76**, 035426.
11 M.W. Knight, N.J. Halas, *New J. Phys.*, 2008, **10**, 105006.
12 R.M. Cole, J.J. Baumberg, F.J. García de Abajo, S. Mahajan, M. Abdelsalam, P.N. Bartlett, *Nano Lett.*, 2007, **7**, 2094.
13 E. Ozbay, *Science*, 2006, **311**, 189.
14 K.F. MacDonald, N.I. Zheludev, *Las. Photon. Rev*. 2010, **4**, 562.

Nanoscale Accepted Manuscript

This journal is © The Royal Society of Chemistry 2016

Please do not adjust margins
View Article Online
DOI: 10.1039/C6NR01317A

Published on 10 May 2016. Downloaded by Middle East Technical University (Orta Dogu Teknik U) on 10/05/2016 10:26:07.

15 A.V. Zayats, I.I. Smolyaninov, J. *Opt. A: Pure and Applied Optics*, 2003, **5**, S16.
16 Y. Zhang, N.K. Grady, C. Ayala-Orozco, N.J. Halas, *Nano Lett*. 2011, **11**, 5519.
17 N.N. Lal, B.F. Soares, J.K. Sinha, F. Huang, S. Mahajan, P.N. Bartlett, J.J.Baumberg,. *Opt. Express*, 2011, **19**, 11256.
18 H.A. Atwater, A. Polman, *Nat. Mater*., **9**, 205–213. (2010).
19 T. Qiu, J. Jiang, W. Zhang, X. Lang, X. Yu, P.K. Chu, *ACS Appl. Mater. Interfaces*, 2010, **2**, 2465.
20 Y.L. Zhang, H. Xia, E. Kim, H.B. Sun, *Soft Matter*, 2012, **8**, 11217.
21 X. Wen, Z. Xi, X. Jiao, W. Yu, G. Xue, D. Zhang, H. Ming *Plasmonics* 2013, **8**, 225.
22 C. Schäfer, D.P. Kern, M. Fleischer, *Lab on a Chip*, 2015, **15**, 1066.
23 X. Lang, T. Qiu, W. Zhang, Y. Yin, P.K. Chu, *J. Phys. Chem. C*, 2010, **115**, 24328.
24 P.N. Bartlett, J.J. Baumberg, P.R. Birkin, M.A. Ghanem, M.C. Netti, *Chem. Mater*., 2002, **14**, 2199.
25 S. Dinda, V. Suresh, P. Thoniyot, A. Balčytis, S. Juodkazis, S. Krishnamoorthy, *ACS Appl. Mater. Interfaces*, 2015, **7**, 27661.
26 K.M. Mayer, J.H. Hafner, *Chem. Rev*., 2011, **111**, 3828.
27 F. Korte, J. Koch, B.N. Chichkov, *Appl. Phys. A*, 2004, ***79***, 879.
28 Y. Nakata, T. Okada, M. Maeda, *Jpn. J. Appl. Phys.*, 2003, ***42***, L1452.
29 N.A. Inogamov and V. V. Zhakhovskii, *JETP Lett.*, 2014, **100**, 4.
30 N.A. Inogamov, V.V. Zhakhovskii, V.A. Khokhlov, *JETP*, 2015, **120**, 15.
31 V. Zhakhovskii, K. Nishihara, Y. Fukuda, S. Shimojo, T. Akiyama, S. Miyanaga, H. Sone, H. Kobayashi, E. Ito, Y. Seo, M. Tamura, Y. Ueshima, *IEEE Proceeding of the 5th International Symposium on Cluster Computing and Grid* (CCGrid 2005) 2005, **2**, 848.
32 S. Babar, J.H. Weaver, *Appl. Opt*., 2015, **54**, 477.
33 C. Unger, J. Koch, L. Overmeyer, B.N. Chichkov, *Opt. Express* 2012, **20**, 24864.
34 Y. Nakata, N. Miyanaga, K. Momoo, T. Hiromoto, *Appl. Surf. Sci*., 2013, **274**, 27.
35 Y.P. Meshcheryakov, N.M. Bulgakova, *Appl. Phys. A*, 2006, **82**, 363.
36 A. Kuchmizhak, S. Gurbatov, O. Vitrik, Y. Kulchin, V. Milichko, S. Makarov , S. Kudryashov,. *Sci. Rep*., 2016, **6**, 19410.
37 J.M. Liu, *Opt. Lett*. 1982, **7**, 196.
38 Yu.N. Kulchin, O.B. Vitrik, A.A. Kuchmizhak, A.G. Savchuk, A.A. Nepomnyashchii, P.A. Danilov, D.A. Zayarnyi, A.A. Ionin, S.I. Kudryashov, S.V. Makarov, A.A. Rudenko, V.I. Yurovskikh, A.A. Samokhin, *JETP* 2014, **119**, 15.
39 G. Bernard, C.H.P. Lupis, *Metall. Trans.*, 1971, **2**, 555.
40 I. Egry, G. Lohoefer, G. Jacobs, *Phys. Rev. Lett.*, 1995,**75** 4043.
41 U. Zywietz, A.B. Evlyukhin, C. Reinhardt, and B. N. Chichkov, *Nat. Commun*. 2014, **5**, 3402.
42 P. Dmitriev, S.V. Makarov, V. Milichko, I. Mukhin, A. Gudovskikh, A. Sitnikova, A. Samusev, P. Belov, *Nanoscale* 2016. DOI: 10.1039/C5NR06742A
43 D. Shen, G. Zou, L. Liu, W.W. Duley, Y.N. Zhou, *Soft Matter*, 2016, **12**, 295-301.
44 N.S. King, Y. Li, C. Ayala-Orozco, T. Brannan, P. Nordlander, N.J. Halas, *ACS Nano*, 2011, **5**, 7254.
45 M. Cortie, M.A. Ford, *Nanotechnol*. 2007, **18**, 235704.
46 J.B. Lassiter, M.W. Knight, N.A. Mirin, N.J. Halas, *Nano Lett*., 2009, **9**, 4326.
47 J.R. Lakowicz, C.D. Geddes, I. Gryczynski, J.B. Malicka, Z. Gryczynski, K. Aslan, J.A. Huang, In Biomedical Optics (2004).
48 E.C. Le Ru, P.G. Etchegoin, J. Grand, N. Felidj, J. Aubard, G. Levi, *J. Phys. Chem. C*, 2007, **111**, 16076.
49 J.R. Lakowicz, *Anal. Biochem*., 2004, **324**, 153.
50 C. D. S. Brites, P. P. Lima, N. J. O. Silva, A. Millán, V. S. Amaral, F. Palacio and L. D. Carlos, *Nanoscale*, 2012, **4**, 4799.
51 J.I. Kato, N. Takeyasu, Y. Adachi, H.B. Sun, S. Kawata, *Appl. Phys. Lett*., 2005, **86**, 044102.
52 S. Matsuo, S. Juodkazis, H. Misawa, *Appl. Phys. A*, 2005, **80**, 683.

Nanoscale Accepted Manuscript

Please do not adjust margins